Journal of
Materials Chemistry A

PAPER

View Article Online
View Journal | View Issue

Check for updates

Cite this: *J. Mater. Chem. A*, 2025, **13**, 4237

Elucidating the effects of bromine substitution in asymmetric quinoxaline central core-based non-fullerene acceptors on molecular stacking and photovoltaic performances†

Dingding Qiu,‡[a] Liting Zhang,‡[a] Hao Zhang,[a] Ailing Tang,[a] Jianqi Zhang,[a] Zhixiang Wei *[ab] and Kun Lu *[ab]

Received 8th November 2024
Accepted 20th December 2024

DOI: 10.1039/d4ta07953a

rsc.li/materials-a

Substitution optimization is an efficient method to construct non-fullerene acceptors (NFAs), and electronegative fluorine and chlorine are generally used for this. However, the research on bromine, which is a larger atom, is scarce. Herein, we synthesized five NFAs with different substitutions to elucidate the effect of bromine substitutions (alkoxy, hydrogen, chlorine, and fluorine were also tested for comparison) based on an asymmetric quinoxaline central core. A novel method involving the local surface electrostatic potential (local ESP) was developed to compare the various electron properties. The results showed that the intrinsic characteristics of bromine, including its large atomic radius, strong polarizability, and weak electronegativity, led to a slightly enhanced local-ESP value of the central core in the brominated NFA (Qx-PhBr), which directly guided the molecular stacking, as proved by the single-crystal analysis. Simultaneously, the donor–acceptor interaction was also weakened due to the bromine substitution. As a result, Qx-PhBr demonstrated tight molecular stacking and an optimized blend film morphology and achieved an excellent PCE of 19.65% in binary organic solar cells. Meanwhile, the optimal molecular stacking and interactions also endowed this efficient system with excellent stability and tolerance to film-thickness. This work emphasizes the potential of brominated NFAs and proposes an innovative method of utilizing the local ESP.

Introduction

Organic solar cells (OSCs) have emerged as a promising photovoltaic technology over the past two decades, with several beneficial features, including low cost, light weight, and mechanical flexibility.[1–5] With the continuous and excellent advances in molecular design and device fabrication engineering,[6–10] up to 20% power conversion efficiencies (PCEs) have now been achieved in single-junction OSCs. This excellent progress largely depends on the continuous development of non-fullerene small molecular acceptors (NFAs).[11–20] Generally, the active layer of OSCs promote efficient carrier transport and optimized bulk heterojunction structures for achieving outstanding performances,[21–25] which sets extremely high requirements for the fine regulation of molecular stacking in NFAs.[26–28] Therefore, an in-depth study of the conjunction and aggregation of NFAs is essential.[29–32]

The crystallization behaviour and aggregation structure of NFAs fundamentally stem from the various intermolecular interactions, which mainly include π–π interactions and non-covalent interactions.[33–35] The π–π interactions originate from the overlap of the π electron orbitals of the conjugated molecules, so the configuration and range of π-conjugated skeletons in NFAs would significantly impact the interaction and stacking modes.[36–38] The excellent performances of Y-series acceptors, such as Y6 and L8-BO, largely depend on their banana-shaped structure, which helps to form a three-dimensional (3D) stacking mode and transport channel.[39,40] In the development of Y-series acceptors, the asymmetric strategy is a simple but effective method to significantly regulate the conjugated skeletons, thus leading to significantly improved molecular stacking, a largely broadened material library, and remarkably improved device performances.[41–44] Asymmetric acceptors can be structurally classified into three categories; molecules with an asymmetric end group, asymmetric backbone, or asymmetric side chain.[45–47] For the central core units that have been frequently modified recently,[48,49] the asymmetric strategy has been rarely utilized, which is largely due to the lack of

---

[a] *CAS Key Laboratory of Nanosystem and Hierarchical Fabrication, CAS Center for Excellence in Nanoscience, National Center for Nanoscience and Technology, Beijing 100190, China. E-mail: weizx@nanoctr.cn; lvk@nanoctr.cn*

[b] *University of Chinese Academy of Sciences, Beijing 100049, China*

† Electronic supplementary information (ESI) available. CCDC 2299124. For ESI and crystallographic data in CIF or other electronic format see DOI: https://doi.org/10.1039/d4ta07953a

‡ These authors contributed equally.

modification sites in the central cores of benzothiadiazole (BTz) in Y-series acceptors. On the contrary, the quinoxaline (Qx)-series acceptors reported by our group could deliver abundant chemical modification sites on the central core,[50,51] so we believe that utilizing the Qx central core with an asymmetric structure is a promising but under-researched method to construct efficient acceptor materials.

On the other hand, the non-covalent interactions in NFAs are mainly derived from the heteroatoms connected to the conjugated skeleton.[52–55] Strongly electron-negative halogen atoms (such as F and Cl) have empty valence orbitals that can accept lone-pair electrons from electron-rich atoms (such as S and O) to induce strong interactions.[56–58] Therefore, simply introducing some substituents could provide rich non-covalent interactions, which would further modify the planarity and rigidity of the conjugate skeletons, expand the regulation of the material properties, such as the absorption and energy levels, and optimize the film morphology and device performance.[59–63] In addition, the introduction of halogen atoms or an alkoxy group would also have an undeniable influence on the π electron cloud of the conjugated skeleton due to the electronic effects of these substituents.[64,65] The enhanced intermolecular charge-transfer (ICT) effect would further enhance the absorption characteristics of the material and assist in charge separation in blend films, thereby improving device performance.[66,67]

In this work, based on Qx-series acceptors, we synergistically utilized the central unit asymmetry and non-covalent interaction strategies to synthesize five novel acceptor materials: Qx-PhOR (with ethoxy group substitution), Qx-Ph (with an unsubstituted single phenyl), Qx-PhBr, Qx-PhCl, and Qx-PhF. The unique asymmetric central cores with a substituted or unsubstituted single phenyl significantly affected the molecular configuration, electron distribution, molecular stacking mode, and aggregation state morphology. As a result, the five acceptors delivered systematically regulated light absorption, bandgap, and energy levels, displaying considerable potential to improve device performance. These factors together contributed to the gradual optimization of the performances of devices fabricated with these materials, in which Qx-PhBr-based OSCs with PM6 as the polymer donor exhibited an excellent PCE of 18.62%, along with superior thermal stability. More excitingly, an impressive efficiency of 19.65% was reached when replacing the PEDOT:PSS with 2PACz as the hole-transport layer. In addition, the optimal molecular interactions of the Qx-PhBr-based blend films inspired us to test the film-thickness tolerance of this system, and an encouraging PCE of 15.71% was achieved after thickening the active layers to about 500 nm. Our work highlights the great potential of the asymmetric central cores in NFAs through systematically adjusting π–π interactions and the non-covalent interactions.

Results and discussion

Fig. 1a shows the molecular structures of the five NFAs with asymmetric central cores, for which the detailed synthetic routes and procedures are illustrated in Scheme S1, ESI.† The chemical structures of the five molecules were characterized by ^{1}H NMR and MALDI-TOF techniques, and the results are shown in Fig. S1–45.† All five NFAs exhibited good solubility in common organic solvents, including chloroform, toluene, and chlorobenzene, which is beneficial for solution processing and device fabrication. As shown in Fig. 1b, compared with Qx-Ph with an unsubstituted single phenyl, the central cores for the other four NFAs delivered significantly increased dipole moments, which is conducive to obtaining enhanced intermolecular interactions and tighter molecular stacking. The exciton binding energy (E_b) of the five NFAs were also measured and calculated, and the method utilized and the results are shown in the ESI.† It can be seen from Fig. S46 and Table S1† that the four NFAs with substituents had lower E_b values compared with Qx-Ph, which matched well with the enhanced central core dipole moments. As for the differences between the four NFAs with substituents, the E_b results were not completely consistent with their central core dipole moments, which may be due to the various molecular stacking modes, which will be discussed later.

As exhibited in Fig. 1c and d, the UV-vis absorption spectra of the five NFAs in dilute chloroform solution and in the film state were measured to explore the molecular absorption properties, and the corresponding data are summarized in Table S2.† In the solution state, Qx-PhOR, Qx-Ph, Qx-PhBr, Qx-PhCl, and Qx-PhF exhibited various maximum absorption peaks at 744, 739, 735, 736, and 736 nm, respectively, indicating a red/blue shift of the absorption spectrum after central core substitution by an electron-donating/electron-withdrawing group. All four NFAs with various substituents linked on the phenyl group delivered increased ε values compared with Qx-Ph without a substituent on the phenyl group, which was due to the enhanced intermolecular charge-transfer effects induced by the electronic properties of the substituents. For the three NFAs with electron-withdrawing substituents (Qx-PhBr, Qx-PhCl, and Qx-PhF), stronger electronic property led to greater absorption. In the film state, the four NFAs with substituents still delivered large ε values compared with Qx-Ph, albeit there were significant differences among them, which may be due to their different molecular stacking and crystallinity. From the solution to the film state, the five molecules showed significant differences in the red-shift of their maximum absorption peaks (see Fig. 1e), and all four NFAs with substituents on the phenyl group delivered blue-shifted absorption spectra regardless of the electronic effects of the substituents, indicating potential differences in the molecular stacking of the four NFAs induced by the substitution on the phenyl group, which will be discussed later. In addition, the films of Qx-PhOR, Qx-PhBr, Qx-PhCl, and Qx-PhF exhibited obviously expanded absorption spectra compared with Qx-Ph, which could be attributed to the enhanced ICT effect, which would be beneficial for improving the current density in the corresponding OSC devices. Moreover, all five NFAs showed complementary absorption spectra with the polymer donor PM6, illustrating their suitability for constructing OSC devices. These results demonstrate that the substitution groups on the central core of the five asymmetric NFAs significantly affect the optical properties of the NFAs.

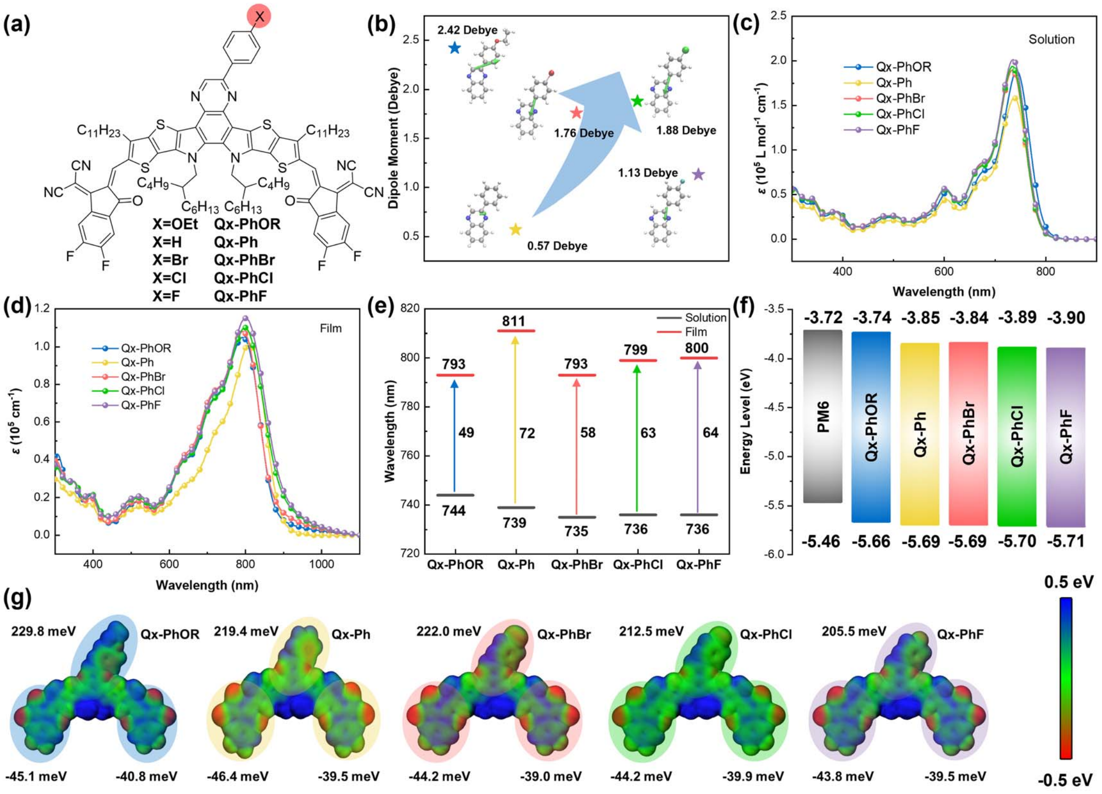

Fig. 1 (a) Molecular structures of the five NFAs. (b) Central core dipole moments of the five NFAs obtained by density functional theory (DFT) calculations. (c) Absorption coefficient (ε) of the five NFAs in dilute chloroform solution. The concentration was 8 μg mL^{-1}. (d) Absorption coefficient (ε) of the five NFAs in the film state. The film thickness was obtained through a stylus profilometer (KLA-Tencor D-120). (e) Change of the maximum absorption peak positions from the solution to the film state of the five NFAs. (e) Energy levels of the five NFAs calculated from cyclic voltammetry (CV) measurements, in which the solvent was acetonitrile, the reference electrode was a Ag+/Ag electrode, the counter electrode was a Pt plate, and the electrolyte was tetrabutylammonium phosphorus hexafluoride (Bu_4NPF_6). (g) Local ESP analysis of the five NFAs obtained by density functional theory (DFT) calculations.

Next, cyclic voltammetry (CV) measurements were conducted to determine the highest occupied molecular orbital (HOMO) and the lowest unoccupied molecular orbital (LUMO) energy levels of the five NFAs (Fig. S47†). According to the oxidation and reduction onsets, the HOMO/LUMO energy levels of Qx-PhOR, Qx-Ph, Qx-PhBr, Qx-PhCl, and Qx-PhF were calculated to be −5.66/−3.74, −5.69/−3.85, −5.69/−3.84, −5.70/−3.89, and −5.71/−3.90 eV, respectively, as shown in Fig. 1f. The gradually downshifted HOMOs from Qx-PhOR to Qx-Ph, Qx-PhBr, Qx-PhCl, and Qx-PhF could be ascribed to the gradually weakened electron-donating effect (or enhanced electron-withdrawing effect) of the corresponding substitution groups. Meanwhile, the energy gaps derived from the CV measurements were calculated to be 1.92, 1.84, 1.85, 1.81, and 1.81 eV for Qx-PhOR, Qx-Ph, Qx-PhBr, Qx-PhCl, and Qx-PhF, respectively, which agree well with the different absorption spectra mentioned above. Noting that Qx-PhBr delivered a slightly upshifted LUMO compared with Qx-Ph despite the presence of electronegative bromine on the central core, it was necessary to explore the detailed effect of the central core substitution on the material properties.

It is known that molecular surface electrostatic potential (ESP) can intuitively reflect the electronic properties of molecules and significantly affect the intermolecular interactions and molecular stacking,[68,69] so ESP analysis of the five NFAs was simulated by DFT to investigate the detailed differences in the molecular charge distribution among the five molecules. Fig. S48† shows the ESP distributions of the five NFAs, for which the ESP quantified parameters are summarized in Table S3.† The central cores of the five NFAs showed slightly distinctive colours in the ESPs, while the differences in the end groups were negligible. Considering the important role of the central cores in molecular stacking, the local ESP distributions were analysed to explore the charge distribution in the local regions of the whole molecules. As illustrated in Fig. 1g and Table S4,† the local ESP overall average values of the central cores in all five NFAs were positive, while the local ESP overall average values of the end groups were negative, indicating the tendency of stacking between them. The local ESP overall average values of the end groups in the five NFAs were similar at about −42 meV, whereas the local ESP overall average values of the central cores showed obvious differences. Compared with Qx-Ph, the central core of Qx-PhOR with ethoxy group substitution delivered an enhanced ESP average value (229.8 meV *vs.* 219.4 meV), indicating the increased electron cloud density, which could be attributed to the strong electron-donating property of the ethoxy group. The electronegative chlorine and fluorine on the central cores of Qx-PhCl and Qx-PhF also resulted in smaller local ESP average values (212.5 and 205.5 meV) compared with Qx-Ph. As for Qx-PhBr, however, despite the electronegative bromine on the central core, it exhibited a slightly increased local ESP average value of 222.0 meV, which may be due to the weakest electron-withdrawing property, and smaller electronegativity of bromine, its largest atomic radius, and strongest polarizability. The larger differences between the local ESP average values for the central cores and the end groups in Qx-PhOR and Qx-PhBr may have resulted in stronger "E/C" ("E" represents "end groups" and "C" represents "central cores") interactions, which will be discussed in the following part with the single-crystal analysis. In addition, the ESP area distribution was also calculated to explore the degree of dispersion of the charge distribution in the five NFAs. As shown in Fig. S49 and Table S3,† Qx-PhBr delivered the highest proportion between 0 and 500 meV, indicating its reduced ESP distribution disorder, indicating Qx-PhBr has the largest possibility to interact with others through positive and negative ESP regions with a similar extent, while also being beneficial for molecular interactions. These results evidently show that the substitution on the central cores of the five asymmetric molecules significantly affects the electronic properties of the NFAs, which would further influence the molecular stacking and performances of devices fabricated with these NFAs.

In order to unveil the effects of the central core substitution in asymmetric NFAs on their molecular packing behaviours, single-crystal X-ray diffraction measurements were performed. Single crystals of Qx-PhOR were obtained using a slow solvent diffusion method, and the detailed X-ray parameters and checked files can be found in Table S5, Fig. S50, and ESI File 1.† As illustrated in Fig. 2a, Qx-PhOR exhibited a honeycomb-like molecular packing structure. Along the molecular stacking direction (*b*-axis), three types of dimers with different molecular overlaps were found. Dimer 1 and dimer 3 come from the strong π–π interactions between the IC end group and the alkoxy-substituted central cores (E/C), which is consistent with the local ESP analysis results mentioned above, while dimer 2 was formed through the interactions between adjacent IC end

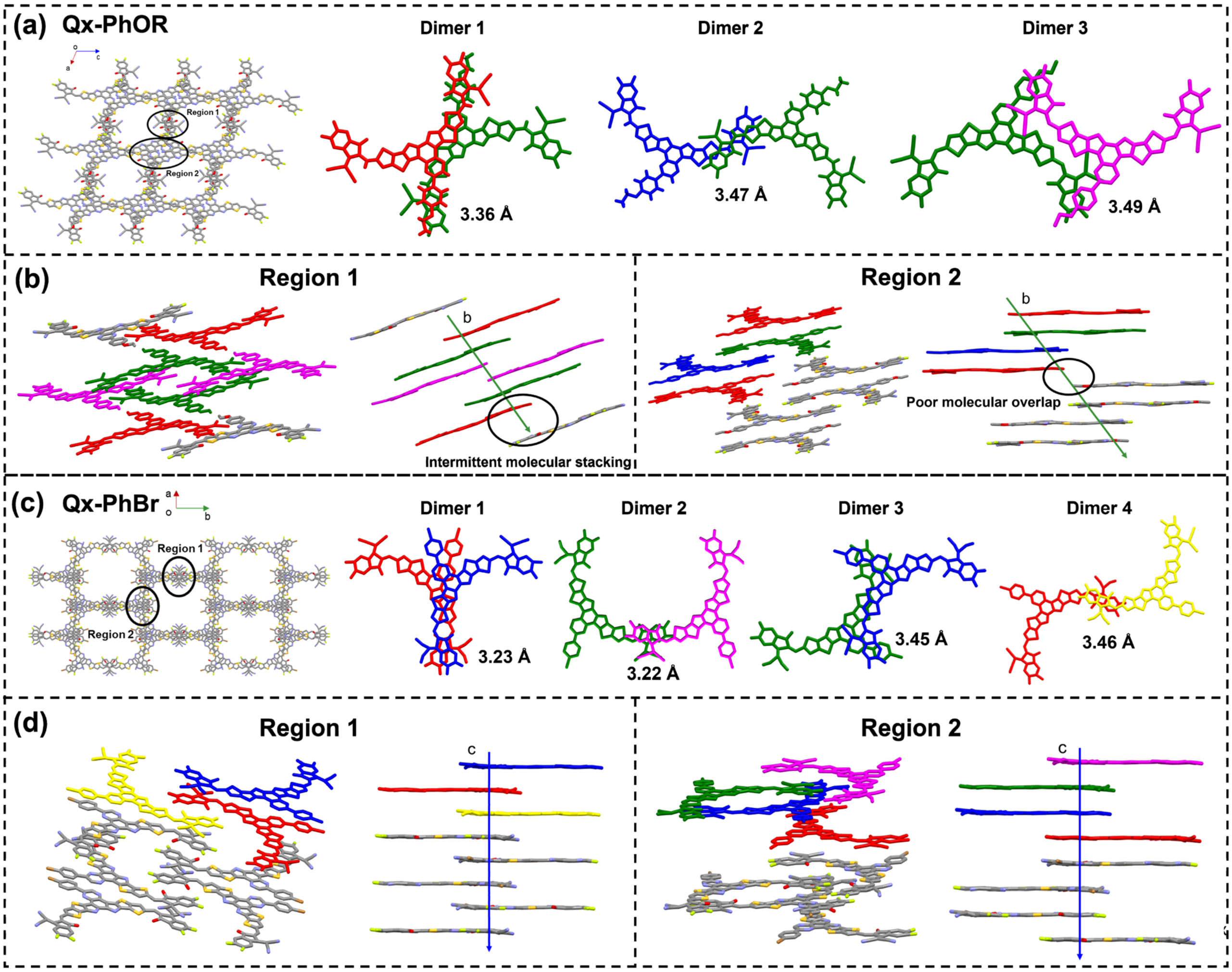

Fig. 2 Single-crystal analysis of Qx-PhOR and Qx-PhBr. Single-crystal structure overview, intermolecular dimeric packing, and stacking distances of (a) Qx-PhOR and (c) Qx-PhBr. Inter-layer molecular overlap and carrier transporting channel analysis of (b) Qx-PhOR and (d) Qx-PhBr.

groups (E/E). Fig. 2b shows how the molecule forms the honeycomb-like molecular packing structure of Qx-PhOR through the three types of dimers, as well as showing the inter-layer carrier-transporting channels. It can be seen from Fig. 2b that both in region 1 and region 2, the inter-layer carrier-transporting channels were insufficient due to the intermittent molecular stacking and poor molecular overlap (as illustrated in the black circles). Therefore, Qx-PhOR cannot form a well-connected framework along the stacking direction, which is unfavourable for effective carrier transport.

For Qx-PhBr, although the complete single-crystal structure was not resolved due to the small size of the crystal, its molecular backbone stacking modes were analysed and can be clearly seen (see ESI File 2†). As shown in Fig. 2c, the backbone stacking mode of Qx-PhBr was also explored using the same method as for Qx-PhOR. It was found that Qx-PhBr delivered four types of dimers: dimer 3 for E/C interactions, and the other three types for E/E interactions. As exhibited in Fig. 2d, the inter-layer carrier-transporting channels were also analysed by investigating the molecular stacking situation along the *c*-axis direction. In region 1, the Qx-PhBr molecule could form neat and tight π–π stacking through dimer 1 and dimer 4 with favourable end group overlaps. In region 2, dimer 1, dimer 2, and dimer 3 combined to construct efficient carrier-transporting channels through the end groups and central cores. In addition, the stacking distances of the E/C mode in Qx-PhOR (dimer 1) were smaller than that in Qx-PhBr (dimer 3), which matched well with the local ESP analysis results. Furthermore, the stacking distances of the E/E mode in Qx-PhBr were smaller than that in Qx-PhOR, suggesting tighter molecular stacking, which is beneficial for remote charge transport. Overall, although both Qx-PhOR and Qx-PhBr could form 3D molecular stacking frameworks, the excessive E/C stacking and insufficient E/E stacking due to the strong electron-donating alkoxy substitution in Qx-PhOR led to inefficient inter-layer carrier-transporting channels. For Qx-PhBr, the favourable electron properties of the bromine atom helped optimize the molecular stacking, resulting in efficient 3D carrier transport, which would be beneficial for device performance.

To further compare the molecular stacking among the five NFAs in the aggregation state, grazing-incidence wide-angle X-ray scattering (GIWAXS) characterizations of the pure NFA films were performed. As exhibited in Fig. S51,† all five NFAs delivered clear dominant face-on orientations. Moreover, the π–π stacking (010) peaks in the out-of-plane (OOP) direction in the GIWAXS results were also considered to calculate π–π stacking distances (*d*-spacing) of the five NFAs in the pure films. As shown in Fig. S52 and Table S6,† the *d*-spacing values were determined to be 3.66, 3.67, 3.63, 3.65, and 3.65 Å for Qx-PhOR, Qx-Ph, Qx-PhBr, Qx-PhCl, and Qx-PhF, respectively, indicating that Qx-PhBr could achieve the tightest molecular stacking among the five NFAs, which matched well with the single-crystal analysis results. Besides, the crystal coherence lengths (CCLs) of the π–π stacking (010) peaks were also calculated, and were 31.07, 27.99, 29.61, 31.07, and 32.31 Å for the five NFAs in the same order, indicating the enhanced crystallinity of the four NFAs with substituents on the central cores. Meanwhile, atomic force microscopy (AFM) measurements of the pure films were also implemented to explore the aggregation ability of the five NFAs. As illustrated in Fig. S53,† the four NFAs with central core substitutions exhibited significantly enhanced root-mean-square (RMS) roughness values compared with Qx-Ph, which was due to the improved intermolecular interactions induced by the substituents. Qx-PhBr showed a favourable aggregation ability with a moderate RMS of 1.18 nm, which was consistent with the medium CCL value obtained in the GIWAXS results and would assist the formation of an optimal blend film morphology in corresponding devices.

The various electronic properties and molecular stacking of the five NFAs inspired us to explore their photovoltaic performances. Consequently, OSC devices with an architecture of glass/ITO/PEDOT:PSS/active layer/PNDIT-F3N/Ag were fabricated, in which PM6 was blended with the five NFAs to construct the active layers. The device optimization procedures and results are summarized in Tables S7–11.† The *J*–*V* curves and device parameters of the optimal devices are shown in Fig. 3a and Table 1. Devices based on the five NFAs yielded V_{OC} values from high to low of 0.904, 0.889, 0.886, 0.880, and 0.872 V for Qx-PhOR, Qx-Ph, Qx-PhBr, Qx-PhCl, and Qx-PhF, respectively, fitting well with their various energy levels, while the J_{SC} values of the five systems showed a converse order compared with the V_{OC} values. The Qx-PhOR-based devices generated a modest PCE of 16.79% despite having the highest V_{OC}, which was due to their unsatisfactory J_{SC} and FF of 24.48 mA cm^{-2} and 75.84%. For Qx-Ph, Qx-PhCl, and Qx-PhF, thanks to the increased J_{SC} and FF compared with Qx-PhOR, PCEs over 18% were obtained in the three binary systems. More excitingly, a champion PCE of 18.62% was achieved by the PM6:Qx-PhBr-based OSC with a V_{OC} of 0.886 V, J_{SC} of 25.80 mA cm^{-2}, and an outstanding FF of 81.45%. Noting that a slightly low J_{SC} was the key factor limiting the PCE of this system, the self-assembled monolayer 2PACz with higher optical transmittance was utilized as the hole-transport layer (see Fig. S54†), and an unexpected PCE of 19.65% was achieved, which rank it among the current first-class OSCs. Fig. 3b displays a scatter chart of the FF and $V_{OC} \times J_{SC}$ values distribution from 16 independently measured devices of the five binary systems (the detailed device parameters are summarized in Tables S12–17†), undoubtedly proving the superior device performances of the Qx-PhBr-based OSCs. The corresponding external quantum efficiency (EQE) curves of the OSCs based on the five NFAs are displayed in Fig. 3c, from which the integrated current density values were calculated and matched well with those afforded by the *J*–*V* tests. The four NFAs with central core substitutions exhibited a blue-shifted EQE onset compared with Qx-Ph, which was consistent with their blue-shifted absorption. Qx-PhBr, Qx-PhCl, and Qx-PhF showed overall higher EQE responses in the wavelength range of 450–850 nm, contributing to the larger integrated current densities of the devices. The 2PACz-based devices delivered an EQE curve with a different shape and strong response, which was attributed to its different spectral transmittance compared with PEDOT:PSS.

The exciton-dissociation and charge-recombination properties in blend films were then investigated to explore the reason

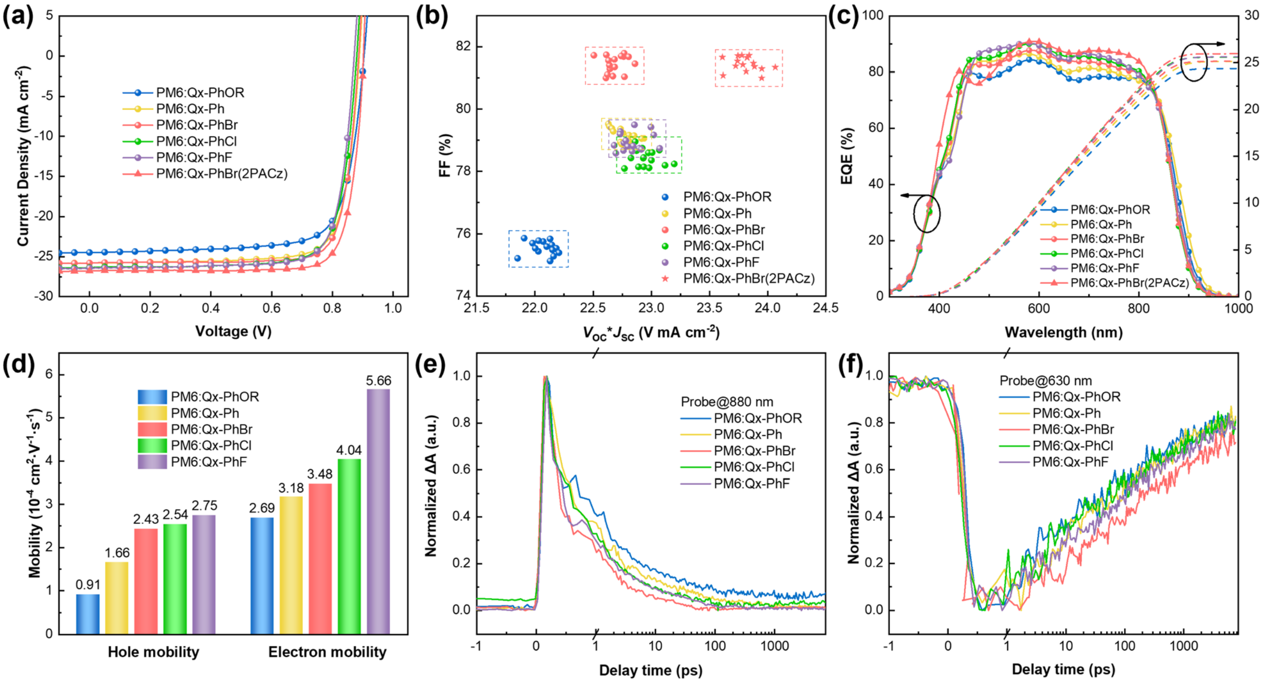

Fig. 3 (a) J–V curves, (b) FF and $V_{OC} \times J_{SC}$ values distribution scatter chart, and (c) EQE curves of the devices. (d) Histograms of the hole and electron mobility of the blend films. Transient kinetic traces probed at (e) 880 nm and (f) 630 nm for the blend films.

Table 1 Photovoltaic metrics of OSCs with different photoactive layers. The average values and standard deviations were obtained from statistical analysis of 16 individual devices

Active layer	V_{OC} (V)	J_{SC} (mA cm^{-2})	Cal. J_{SC}^{a} (mA cm^{-2})	FF (%)	PCE^b (%)
PM6:Qx-PhOR	0.904 (0.905 ± 0.002)	24.48 (24.40 ± 0.09)	24.37	75.84 (55.55 ± 0.21)	16.79 (16.68 ± 0.08)
PM6:Qx-Ph	0.889 (0.890 ± 0.001)	25.80 (25.60 ± 0.10)	25.13	79.06 (79.16 ± 0.20)	18.14 (18.02 ± 0.05)
PM6:Qx-PhBr	0.886 (0.886 ± 0.001)	25.80 (25.61 ± 0.09)	25.15	81.45 (81.44 ± 0.27)	18.62 (18.48 ± 0.10)
PM6:Qx-PhCl	0.880 (0.880 ± 0.002)	26.36 (26.08 ± 0.13)	25.58	78.24 (78.43 ± 0.25)	18.19 (18.01 ± 0.10)
PM6:Qx-PhF	0.872 (0.871 ± 0.002)	26.40 (26.21 ± 0.12)	25.61	79.17 (78.94 ± 0.28)	18.21 (18.03 ± 0.12)
PM6:Qx-PhBr^b	0.902 (0.901 ± 0.002)	26.79 (26.44 ± 0.14)	25.95	81.34 (81.45 ± 0.23)	19.65 (19.39 ± 0.12)

[a] Current density calculated from the EQE spectra. [b] Devices with 2PACz as the hole-transport layer.

for the different device performances of the five NFAs. Fig. S55a† displays the dependence of the photocurrent density (J_{ph}) on the effective voltage (V_{eff}), and the calculated results are summarized in Table S18.† The PM6:Qx-PhBr-based devices yielded the highest values for the efficiencies for exciton dissociation (P_{diss}, 98.69%) and charge collection (P_{coll}, 88.80%), partially explaining the superior device performance. Next, the light intensity (P_{light})-dependent J–V curves were obtained to study the charge-recombination behaviours of the five systems. As depicted in Fig. S55b and S55c,† the PM6:Qx-PhBr-based devices exhibited the largest α value in the plots of log J_{SC} *versus* log P_{light} according to the function $J_{SC} \propto (P_{light})^{\alpha}$, and the smallest slope value fitted from the plots of V_{OC} *versus* ln(P_{light}), indicating the lower charge-recombination behaviours in the devices based on Qx-PhBr. To understand the various J_{SC} and FF values of the devices based on the five NFAs, the electron and hole mobilities (μ_e and μ_h) of their blend films were characterized by the SCLC method (Fig. S56†), and the results are listed in Fig. 3d and Table S18.† The μ_e/μ_h values showed a gradually increasing trend from $0.91 \times 10^{-4}/2.69 \times 10^{-4}$ to $1.66 \times 10^{-4}/3.18 \times 10^{-4}$, $2.43 \times 10^{-4}/3.48 \times 10^{-4}$, $2.54 \times 10^{-4}/4.04 \times 10^{-4}$, and $2.75 \times 10^{-4}/5.66 \times 10^{-4}$ for the Qx-PhOR-, Qx-Ph-, Qx-PhBr-, Qx-PhCl-, and Qx-PhF-based blend films. It could also be seen that the mobilities gradually increased from Qx-PhOR to Qx-Ph, Qx-PhBr, Qx-PhCl, and Qx-PhF, which may be due to the gradually enhanced electron-withdrawing properties of the central cores in the NFAs resulting in a gradual increase in their molecular stacking. For Qx-PhBr, although the J_{SC} value was only moderate, the balanced electron and hole mobilities led to the device demonstrating a superior FF, therefore achieving excellent device performances. The different μ_e/μ_h values could partially explain the various carrier recombinations mentioned above, which are generally considered to be due to the film morphology and will be discussed later.

Femtosecond transient absorption spectroscopy (fs-TA) experiments were next performed to understand the charge transfer (CT) and recombination dynamics for the five systems. The exciton spectra of the five NFAs were first obtained by photoexciting their pure films with a pump wavelength at 800 nm and the results are shown in Fig. S57.† It could be seen that the exciton spectra of the five NFAs were similar and consisted of two negative ground-state bleach (GSB) peaks at about 720 nm and 800 nm, and two excited state absorption (ESA) peaks at about 575 nm and 880 nm, respectively. Then the CT behaviours of the blend films were investigated by selectively exciting the acceptors in the blend films at 800 nm. As illustrated in Fig. S58,† all five systems exhibited a strong GSB at 630 nm, which was ascribed to the GSB of the polymer donor PM6, indicating the occurrence of ultrafast hole transfer from the acceptors exciton to PM6 and generating the CT state in the blend films. The kinetic traces of the blend films at 880 and 630 nm were next obtained, which could reflect the hole-transfer channel and CT state lifetime, respectively. As demonstrated in Fig. 3e and f, the Qx-PhBr-based blend films showed the fastest acceptor exciton decay and the longest CT state lifetime, suggesting efficient hole transfer and lower charge recombination, which could assist achieving a superior FF in the corresponding devices and support superior device performances.

It is generally considered that the morphology of blend films in OSCs would exert a crucial influence on the charge-transport behaviour and photovoltaic performance. Therefore, AFM and transmission electron microscopy (TEM) measurements were performed to reveal the nanoscale morphology of the five NFAs-based blend films. As shown in Fig. 4a and S59,† all the blend films delivered uniform surfaces with fibre-like structures. The values of RMS roughness from the AFM images were determined to be 1.02, 0.96, 1.05, 1.10, and 1.24 nm for the Qx-PhOR-, Qx-Ph-, Qx-PhBr-, Qx-PhCl-, and Qx-PhF-based blend films, respectively, displaying the same trend as that of the pure films mentioned above. It could also be seen from the AFM and TEM images that domain sizes from small to large were obtained for the five NFAs-based blend films in the same order as above. Considering the differences between their domain size and crystallinity, the contact angles (CAs) and derived Flory–Huggins interaction parameters (χ_{DA}) of the five NFAs with PM6 were evaluated to examine the interactions between the donors and acceptors. As displayed in Fig. S60 and Table S19,† the χ_{DA} values were calculated to be 0.36, 0.48, 0.54, 0.47, and 0.40 for Qx-PhOR, Qx-Ph, Qx-PhBr, Qx-PhCl, and Qx-PhF, respectively. The smallest χ_{DA} value between PM6 and Qx-PhOR indicated its highest D/A miscibility and strongest D/A interactions, which, along with the strong crystallinity of Qx-PhOR, led to the Qx-PhOR-based blend films demonstrating the smallest domain size. For Qx-PhBr, its largest χ_{DA} value of 0.54 indicated its lower D/A miscibility. The weak interaction between Qx-PhBr and PM6 and the optimal aggregation ability of Qx-PhBr synergistically resulted in a moderate domain size and relatively high phase purity of the Qx-PhBr-based blend films, which may explain the efficient charge generation/transport and superior FF mentioned above. For Qx-PhCl and Qx-PhF, the strong electron-withdrawing properties of Cl and F atoms led to excessive interactions with the donor PM6, which is disadvantageous for phase separation in device fabrication and was the main reason for their unbalanced mobilities and inferior FF compared with Qx-PhBr.

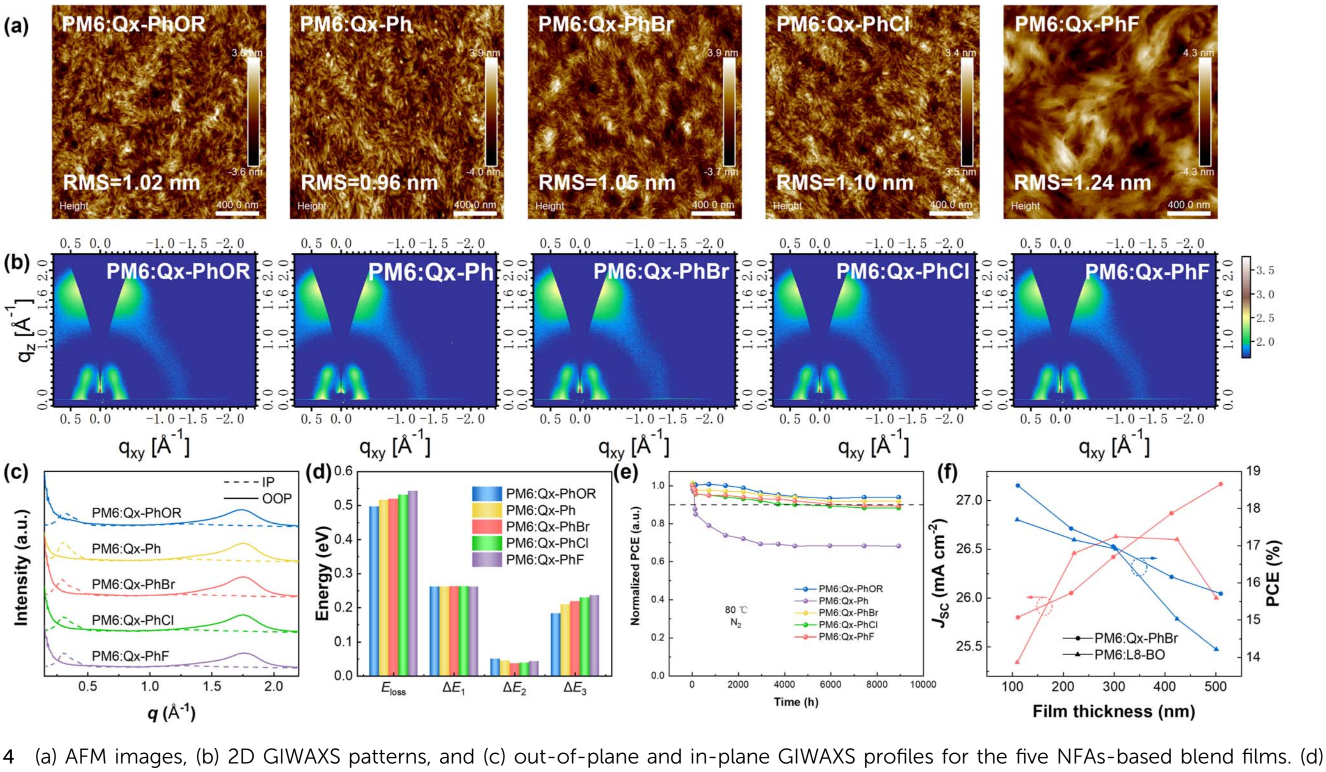

Fig. 4 (a) AFM images, (b) 2D GIWAXS patterns, and (c) out-of-plane and in-plane GIWAXS profiles for the five NFAs-based blend films. (d) Schematic of the energy loss and radiative and nonradiative recombination losses for devices. (e) Thermal stability of the devices. (f) J_{SC} and PCE values of PM6:Qx-PhBr- and PM6:L8-BO-based devices with different thicknesses.

Next, the molecular packing and orientation in the blend films were studied employing GIWAXS measurements. The two-dimensional (2D) GIWAXS patterns of the blend films, the corresponding 1D profiles, and the π–π stacking (010) parameters are presented in Fig. 4b, c, and Table S20.† All the blend films exhibited a dominant face-on orientation with π–π stacking distances (*d*-spacing) of 3.60, 3.58, 3.58, 3.58, and 3.56 Å for the Qx-PhOR-, Qx-Ph-, Qx-PhBr-, Qx-PhCl-, and Qx-PhF-based blend films, respectively. The Qx-PhOR-based blend films delivered the largest *d*-spacing value, which may be due to the strong interactions between Qx-PhOR and PM6 destroying the molecular stacking in the blend films. The CCLs were also calculated to be 24.91, 25.36, 26.42, 27.19, and 27.58 Å for the five NFAs-based blend films with the same order as above. The difference in the CCL values of the five NFAs was in accord with the domain sizes obtained by the AFM and TEM analyses. Overall, the favourable molecular packing and weakened interactions with PM6 of Qx-PhBr endowed its blend films with an optimal morphology and molecular stacking, thus leading to an outstanding FF in the corresponding devices.

Noting the strong correlation between the V_{OC} values in the devices and the central core substitutions in the NFAs, we performed energy loss (E_{loss}) analysis to investigate the reasons for the varied V_{OC} values. According to the Shockley–Queisser (S–Q) limit, the E_{loss} in OSCs can be divided into three parts: ΔE_1, ΔE_2, and ΔE_3, in which ΔE_1 is the inevitable radiative energy loss above the bandgap, ΔE_2 represents the radiative recombination loss below the bandgap, and ΔE_3 is the nonradiative recombination loss. The detailed calculation method was described in the Experimental Section earlier and the results are summarized in Fig. 4d, S61, and Table S21.† The E_{loss} values of the Qx-PhOR-, Qx-Ph-, Qx-PhBr-, Qx-PhCl-, and Qx-PhF-based OSCs were determined to be 0.497, 0.517, 0.520, 0.532, and 0.543 eV, respectively, displaying a gradually increasing trend. Detailed analysis was then conducted to explain this trend. The five systems showed very similar ΔE_1 values of about 0.263 eV but varied ΔE_2 and ΔE_3 values. Considering that ΔE_2 is related with the CT state in the OSCs and corresponds to the driving force required for exciton dissociation, the CT state energies of the five systems were calculated. As shown in Fig. S62,† the Qx-PhBr-based devices displayed the largest CT state energy value of 1.407 eV, agreeing with the smallest ΔE_2 value among the five systems. The ΔE_3 can be calculated by measuring the electroluminescence external quantum efficiency (EQE_{EL}) of the corresponding OSCs. As shown in Table S21,† the ΔE_3 values of the five systems showed a gradual increase from Qx-PhOR to Qx-Ph, Qx-PhBr, Qx-PhCl, and Qx-PhF, indicating that the differences in the central core substitutions and molecular electronic properties could significantly affect the electroluminescent and nonradiative recombination losses in the corresponding OSCs.

Excellent long-range stability is a necessary feature of photovoltaic devices for practical applications. Herein, the thermal stability of the five NFAs-based devices were tested. As shown in Fig. 4e, all four NFAs with substitutions delivered superior device stability compared with Qx-Ph, which may be due to the enhanced intermolecular interactions. The Qx-PhBr-based devices still demonstrated a PCE of 91.90% of the initial PCE after about 9000 h at 80 °C, demonstrating excellent efficiency and stability simultaneously. The roll-to-roll technology utilized in practical applications is always accompanied by an uneven film thickness, which poses a high demand for film-thickness tolerance for efficient OSC systems. Noting the excellent FF of the Qx-PhBr-based devices and the optimal molecular stacking and film morphology, Qx-PhBr could be expected to enable fabricating efficient OSC devices with an enlarged active layer film thickness. Therefore, we fabricated Qx-PhBr-based OSC devices with a gradually increasing active layer thickness from about 100 nm to 500 nm, while the classical efficient system PM6:L8-BO was also tested to compare performances. As shown in Fig. 4f, S63 and Table S22,† the Qx-PhBr-based devices delivered significantly better efficiency maintenance with the enlarged film thickness due to the relatively slow FF decrease and continuously increasing J_{SC}, indicating their considerable potential for roll-to-roll processing and practical applications. The superior thick-film device performances of Qx-PhBr compared with L8-BO were attributed to its high charge-collection efficiency and weak recombination that were also preserved in the thick films, as revealed by Fig. S64 and Table S23.†

Conclusions

Five novel NFAs (Qx-PhOR, Qx-Ph, Qx-PhBr, Qx-PhCl, and Qx-PhF) were constructed with asymmetric central cores, differing only in the central core substitutions, which could modify the material electron properties and molecular stacking. Directed by the asymmetric central cores and the different substituents, the five NFAs delivered various electronic properties, increased dipole moments of the central units, and different molecular aggregation abilities. Local ESP analysis was carried out to quantitatively evaluate the local charge distribution in the whole molecules, which further showed the effects on the molecular stacking mode and distances, proved by the single-crystal analysis and GIWAXS measurement results. Systemic investigations revealed that bromine atom with a modest electronegativity and electron-withdrawing property on the central core could promote tight molecular stacking and favourable crystallinity in Qx-PhBr. As a result, thanks to the superior charge generation/transport dynamics and the optimal blend film morphology, fabricated PM6:Qx-PhBr-based binary OSCs yielded an exceptional PCE of 18.62%, which was further improved to 19.65% through interface engineering with 2PACz as the hole-transport layer. Moreover, excellent thermal stability was also achieved in the Qx-PhBr system, along with a PCE of up to 15.71% after thickening the active layer to about 500 nm, demonstrating the considerable potential of Qx-PhBr for practical applications. Our work shows the great potential of the asymmetric central cores in NFAs and highlights the significance of various substitutions on the central core for adjusting the material's electronic property and molecular stacking.

Data availability

The data supporting this article have been included as part of the ESI.†

Author contributions

D. Q., L. Z., Z. W. and K. L. conceived the idea. D. Q. carried out the device fabrication and measurements. L. Z. synthesized these acceptors and grew the related single crystals. J. Z. performed the GIWAXS measurements. H. Z helped in the DFT calculations. D. Q. prepared the manuscript. A. T. helped in the revision of the manuscript. K. L. and Z. W. directed and supervised the project. All authors discussed and commented on the manuscript.

Conflicts of interest

There are no conflicts to declare.

Acknowledgements

The authors acknowledge the financial support by the Beijing Natural Science Foundation (Grant No. Z230018) and the Strategic Priority Research Program of the Chinese Academy of Sciences (No. XDB0520102), CAS Project for Young Scientists in Basic Research (Grant No. YSBR-102).

Notes and references

1 Y. Shen, H. Zhang, J. Zhang, C. Tian, Y. Shi, D. Qiu, Z. Zhang, K. Lu and Z. Wei, *Adv. Mater.*, 2023, **35**, e2209030.

2 Z. Ling, M. I. Nugraha, W. T. Hadmojo, Y. Lin, S. Y. Jeong, E. Yengel, H. Faber, H. Tang, F. Laquai, A.-H. Emwas, X. Chang, T. Maksudov, M. Gedda, H. Y. Woo, I. McCulloch, M. Heeney, L. Tsetseris and T. D. Anthopoulos, *ACS Energy Lett.*, 2023, 4104.

3 Y. Chang, X. Zhu, L. Zhu, Y. Wang, C. Yang, X. Gu, Y. Zhang, J. Zhang, K. Lu, X. Sun and Z. Wei, *Nano Energy*, 2021, **86**, 106098.

4 L. Ma, S. Zhang, J. Ren, G. Wang, J. Li, Z. Chen, H. Yao and J. Hou, *Angew. Chem., Int. Ed.*, 2023, **62**, e202214088.

5 T. Chen, S. Wang, Z. Yang, Q. Feng, X. Sun, L. Li, Z. S. Wang and H. Peng, *Angew. Chem., Int. Ed.*, 2011, **50**, 1815.

6 M. Zhou, C. Liao, Y. Duan, X. Xu, L. Yu, R. Li and Q. Peng, *Adv. Mater.*, 2023, **35**, e2208279.

7 D. Li, N. Deng, Y. Fu, C. Guo, B. Zhou, L. Wang, J. Zhou, D. Liu, W. Li, K. Wang, Y. Sun and T. Wang, *Adv. Mater.*, 2023, **35**, e2208211.

8 C. Xiao, X. Wang, T. Zhong, R. Zhou, X. Zheng, Y. Liu, T. Hu, Y. Luo, F. Sun, B. Xiao, Z. Liu, C. Yang and R. Yang, *Adv. Sci.*, 2023, **10**, e2206580.

9 H. Chen, S. Y. Jeong, J. Tian, Y. Zhang, D. R. Naphade, M. Alsufyani, W. Zhang, S. Griggs, H. Hu, S. Barlow, H. Y. Woo, S. R. Marder, T. D. Anthopoulos, I. McCulloch and Y. Lin, *Energy Environ. Sci.*, 2023, **16**, 1062.

10 Z. Chen, J. Zhu, D. Yang, W. Song, J. Shi, J. Ge, Y. Guo, X. Tong, F. Chen and Z. Ge, *Energy Environ. Sci.*, 2023, **16**, 3119.

11 H. Yu, Y. Wang, X. Zou, J. Yin, X. Shi, Y. Li, H. Zhao, L. Wang, H. M. Ng, B. Zou, X. Lu, K. S. Wong, W. Ma, Z. Zhu, H. Yan and S. Chen, *Nat. Commun.*, 2023, **14**, 2323.

12 T. Duan, W. Feng, Y. Li, Z. Li, Z. Zhang, H. Liang, H. Chen, C. Zhong, S. Jeong, C. Yang, S. Chen, S. Lu, O. A. Rakitin, C. Li, X. Wan, B. Kan and Y. Chen, *Angew. Chem., Int. Ed.*, 2023, e202308832.

13 Z. Yao, X. Cao, X. Bi, T. He, Y. Li, X. Jia, H. Liang, Y. Guo, G. Long, B. Kan, C. Li, X. Wan and Y. Chen, *Angew. Chem., Int. Ed.*, 2023, e202312630.

14 Z. Zhong, S. Chen, J. Zhao, J. Xie, K. Zhang, T. Jia, C. Zhu, J. Jing, Y. Liang, L. Hong, S. Zhu, D. Ma and F. Huang, *Adv. Energy Mater.*, 2023, e2302273.

15 R. Yu, R. Shi, Z. He, T. Zhang, S. Li, Q. Lv, S. Sha, C. Yang, J. Hou and Z. Tan, *Angew. Chem., Int. Ed.*, 2023, **62**, e202308367.

16 J. Huang, H. Wang, K. Yan, X. Zhang, H. Chen, C. Z. Li and J. Yu, *Adv. Mater.*, 2017, **29**, 1606729.

17 J. Vollbrecht, V. V. Brus, S. J. Ko, J. Lee, A. Karki, D. X. Cao, K. Cho, G. C. Bazan and T. Q. Nguyen, *Adv. Energy Mater.*, 2019, **9**, 1901438.

18 A. Yazmaciyan, M. Stolterfoht, P. L. Burn, Q. Lin, P. Meredith and A. Armin, *Adv. Energy Mater.*, 2018, **8**, 1703339.

19 Y. Wang, X. Wang, B. Lin, Z. Bi, X. Zhou, H. B. Naveed, K. Zhou, H. Yan, Z. Tang and W. Ma, *Adv. Energy Mater.*, 2020, **10**, 1901438.

20 H. Kang, G. Kim, J. Kim, S. Kwon, H. Kim and K. Lee, *Adv. Mater.*, 2016, **28**, 7821–7861.

21 W. Kim, J. Oh, J. Park, Z. Sun, J. Park, T. L. H. Mai, S. Kim and C. Yang, *Nano Energy*, 2023, **117**, 108853.

22 C. Han, J. Wang, S. Zhang, L. Chen, F. Bi, J. Wang, C. Yang, P. Wang, Y. Li and X. Bao, *Adv. Mater.*, 2023, **35**, e2208986.

23 C. Han, J. Wang, L. Chen, J. Chen, L. Zhou, P. Wang, W. Shen, N. Zheng, S. Wen, Y. Li and X. Bao, *Adv. Funct. Mater.*, 2021, **31**, 2107026.

24 Y. Chang, X. Zhu, Y. Shi, Y. Liu, K. Meng, Y. Li, J. Xue, L. Zhu, J. Zhang, H. Zhou, W. Ma, Z. Wei and K. Lu, *Energy Environ. Sci.*, 2022, **15**, 2937.

25 Y. Tang, L. Xie, D. Qiu, C. Yang, Y. Liu, Y. Shi, Z. Huang, J. Zhang, J. Hu, K. Lu and Z. Wei, *J. Mater. Chem. C*, 2021, **9**, 7575.

26 J. Wu, Q. Fan, M. Xiong, Q. Wang, K. Chen, H. Liu, M. Gao, L. Ye, X. Guo, J. Fang, Q. Guo, W. Su, Z. Ma, Z. Tang, E. Wang, H. Ade and M. Zhang, *Nano Energy*, 2021, **82**, 105679.

27 J. S. Park, G. U. Kim, D. Lee, S. Lee, B. Ma, S. Cho and B. J. Kim, *Adv. Funct. Mater.*, 2020, **30**, 2005787.

28 B. Yin, Z. Chen, S. Pang, X. Yuan, Z. Liu, C. Duan, F. Huang and Y. Cao, *Adv. Energy Mater.*, 2022, **12**, 2104050.

29 D. Li, X. Zhang, D. Liu and T. Wang, *J. Mater. Chem. A*, 2020, **8**, 15607.

30 Y. Mao, W. Li, M. Chen, X. Chen, R. S. Gurney, D. Liu and T. Wang, *Mater. Chem. Front.*, 2019, **3**, 1062.

31 C. Guo, D. Li, L. Wang, B. Du, Z. X. Liu, Z. Shen, P. Wang, X. Zhang, J. Cai, S. Cheng, C. Yu, H. Wang, D. Liu, C. Z. Li and T. Wang, *Adv. Energy Mater.*, 2021, **11**, 2102000.

32 K. Liu, Y. Jiang, F. Liu, G. Ran, F. Huang, W. Wang, W. Zhang, C. Zhang, J. Hou and X. Zhu, *Adv. Mater.*, 2023, **35**, e2300363.

33 D. Li, C. Sun, T. Yan, J. Yuan and Y. Zou, *ACS Cent. Sci.*, 2021, **7**, 1787.

34 L. Ye, K. Weng, J. Xu, X. Du, S. Chandrabose, K. Chen, J. Zhou, G. Han, S. Tan, Z. Xie, Y. Yi, N. Li, F. Liu, J. M. Hodgkiss, C. J. Brabec and Y. Sun, *Nat. Commun.*, 2020, **11**, 6005.

35 X. Wang, A. Tang, J. Yang, M. Du, J. Li, G. Li, Q. Guo and E. Zhou, *Sci. China: Chem.*, 2020, **63**, 1666.

36 S. Dai, J. Zhou, S. Chandrabose, Y. Shi, G. Han, K. Chen, J. Xin, K. Liu, Z. Chen, Z. Xie, W. Ma, Y. Yi, L. Jiang, J. M. Hodgkiss and X. Zhan, *Adv. Mater.*, 2020, **32**, e2000645.

37 W. Zheng, J. Liu, Y. Guo, G. Han and Y. Yi, *Adv. Funct. Mater.*, 2021, **32**, 2108551.

38 J. Liu, W. Zheng, G. Han and Y. Yi, *Sol. RRL*, 2021, **5**, 2000780.

39 J. Yuan, Y. Zhang, L. Zhou, G. Zhang, H.-L. Yip, T.-K. Lau, X. Lu, C. Zhu, H. Peng, P. A. Johnson, M. Leclerc, Y. Cao, J. Ulanski, Y. Li and Y. Zou, *Joule*, 2019, **3**, 1140.

40 C. Li, J. Zhou, J. Song, J. Xu, H. Zhang, X. Zhang, J. Guo, L. Zhu, D. Wei, G. Han, J. Min, Y. Zhang, Z. Xie, Y. Yi, H. Yan, F. Gao, F. Liu and Y. Sun, *Nat. Energy*, 2021, **6**, 605.

41 J. Wang, M. Zhang, J. Lin, Z. Zheng, L. Zhu, P. Bi, H. Liang, X. Guo, J. Wu, Y. Wang, L. Yu, J. Li, J. Lv, X. Liu, F. Liu, J. Hou and Y. Li, *Energy Environ. Sci.*, 2022, **15**, 1585.

42 C. Li, H. Fu, T. Xia and Y. Sun, *Adv. Energy Mater.*, 2019, **9**, 1900999.

43 Y. Chen, F. Bai, Z. Peng, L. Zhu, J. Zhang, X. Zou, Y. Qin, H. K. Kim, J. Yuan, L. K. Ma, J. Zhang, H. Yu, P. C. Y. Chow, F. Huang, Y. Zou, H. Ade, F. Liu and H. Yan, *Adv. Energy Mater.*, 2020, **11**, 2003141.

44 J. Shi, Z. Chen, H. Liu, Y. Qiu, S. Yang, W. Song and Z. Ge, *Adv. Energy Mater.*, 2023, **13**, 2301292.

45 C. He, Z. Chen, T. Wang, Z. Shen, Y. Li, J. Zhou, J. Yu, H. Fang, Y. Li, S. Li, X. Lu, W. Ma, F. Gao, Z. Xie, V. Coropceanu, H. Zhu, J. L. Bredas, L. Zuo and H. Chen, *Nat. Commun.*, 2022, **13**, 2598.

46 R. Sun, Y. Wu, X. Yang, Y. Gao, Z. Chen, K. Li, J. Qiao, T. Wang, J. Guo, C. Liu, X. Hao, H. Zhu and J. Min, *Adv. Mater.*, 2022, **34**, e2110147.

47 S. Feng, C. Zhang, Y. Liu, Z. Bi, Z. Zhang, X. Xu, W. Ma and Z. Bo, *Adv. Mater.*, 2017, **29**, 1703527.

48 X. Si, Y. Huang, W. Shi, R. Wang, K. Ma, Y. Zhang, S. Wu, Z. Yao, C. Li, X. Wan and Y. Chen, *Adv. Funct. Mater.*, 2023, e2306471.

49 J. Wang, J. Zhu, C. Li, Y. Lin, Y. Yang, Z. Ma and Y. Lu, *Adv. Funct. Mater.*, 2023, e2304449.

50 Y. Shi, Y. Chang, K. Lu, Z. Chen, J. Zhang, Y. Yan, D. Qiu, Y. Liu, M. A. Adil, W. Ma, X. Hao, L. Zhu and Z. Wei, *Nat. Commun.*, 2022, **13**, 3256.

51 M. Xie, Y. Shi, L. Zhu, J. Zhang, Q. Cheng, H. Zhang, Y. Yan, M. Zhu, H. Zhou, K. Lu and Z. Wei, *Energy Environ. Sci.*, 2023, **16**, 3543.

52 D. Han, Y. Han, Y. Kim, J.-W. Lee, D. Jeong, H. Park, G.-U. Kim, F. S. Kim and B. J. Kim, *J. Mater. Chem. A*, 2022, **10**, 640.

53 Z. P. Yu, Z. X. Liu, F. X. Chen, R. Qin, T. K. Lau, J. L. Yin, X. Kong, X. Lu, M. Shi, C. Z. Li and H. Chen, *Nat. Commun.*, 2019, **10**, 2152.

54 F. Cheng, Y. Cui, F. Ding, Z. Chen, Q. Xie, X. Xia, P. Zhu, X. Lu, H. Zhu, X. Liao and Y. Chen, *Adv. Mater.*, 2023, **35**, e2300820.

55 C. Guan, C. Xiao, X. Liu, Z. Hu, R. Wang, C. Wang, C. Xie, Z. Cai and W. Li, *Angew. Chem., Int. Ed.*, 2023, e202312357.

56 R. Yu, H. Yao, Y. Xu, J. Li, L. Hong, T. Zhang, Y. Cui, Z. Peng, M. Gao, L. Ye, Z. A. Tan and J. Hou, *Adv. Funct. Mater.*, 2021, **31**, 2010535.

57 J. Cameron, A. L. Kanibolotsky and P. J. Skabara, *Adv. Mater.*, 2023, e2302259.

58 C. Li, X. Gu, Z. Chen, X. Han, N. Yu, Y. Wei, J. Gao, H. Chen, M. Zhang, A. Wang, J. Zhang, Z. Wei, Q. Peng, Z. Tang, X. Hao, X. Zhang and H. Huang, *J. Am. Chem. Soc.*, 2022, **144**, 14731.

59 L. Yang, X. Song, J. Yu, H. Wang, Z. Zhang, R. Geng, J. Cao, D. Baran and W. Tang, *J. Mater. Chem. A*, 2019, **7**, 22279.

60 K. Chen, H. Fang, C. Zhao, Q. Fan, L. Ding, H. Yan and W. Ma, *Chem. Eng. J.*, 2022, **446**, 137375.

61 X. Zhang, L. Qin, Y. Li, J. Yu, H. Chen, X. Gu, Y. Wei, X. Lu, F. Gao and H. Huang, *Adv. Funct. Mater.*, 2022, **32**, 2112433.

62 X. Zhang, L. Qin, J. Yu, Y. Li, Y. Wei, X. Liu, X. Lu, F. Gao and H. Huang, *Angew. Chem., Int. Ed.*, 2021, **60**, 12475.

63 X. Wang, H. Lu, Y. Liu, A. Zhang, N. Yu, H. Wang, S. Li, Y. Zhou, X. Xu, Z. Tang and Z. Bo, *Adv. Energy Mater.*, 2021, **11**, 2102591.

64 Q. Yang, D. Hu, M. Kumar, H. Dong, S. Ahmed, P. Huang, Z. Xiao and S. Lu, *Sol. RRL*, 2023, **7**, 2201062.

65 L. Xie, A. Lan, Q. Gu, S. Yang, W. Song, J. Ge, R. Zhou, Z. Chen, J. Zhang, X. Zhang, D. Yang, B. Tang, T. Wu and Z. Ge, *ACS Energy Lett.*, 2022, **8**, 361.

66 B. Zheng, J. Ni, S. Li, Y. Yue, J. Wang, J. Zhang, Y. Li and L. Huo, *Adv. Sci.*, 2022, **9**, e2105430.

67 C. W. Schlenker, K. S. Chen, H. L. Yip, C. Z. Li, L. R. Bradshaw, S. T. Ochsenbein, F. Ding, X. S. Li, D. R. Gamelin, A. K. Jen and D. S. Ginger, *J. Am. Chem. Soc.*, 2012, **134**, 19661.

68 M. Saladina, P. Simón Marqués, A. Markina, S. Karuthedath, C. Wöpke, C. Göhler, Y. Chen, M. Allain, P. Blanchard, C. Cabanetos, D. Andrienko, F. Laquai, J. Gorenflot and C. Deibel, *Adv. Funct. Mater.*, 2020, **31**, 2007479.

69 H. Yao, D. Qian, H. Zhang, Y. Qin, B. Xu, Y. Cui, R. Yu, F. Gao and J. Hou, *Chin. J. Chem.*, 2018, **36**, 491.